Journal of
Synchrotron
Radiation

ISSN 0909-0495

Received 2 February 2011
Accepted 24 February 2011

Effective scavenging at cryotemperatures: further increasing the dose tolerance of protein crystals

Eugenio De la Mora,[a,b] Ian Carmichael[c] and Elspeth F. Garman[a]*

[a]Laboratory of Molecular Biophysics, Department of Biochemistry, University of Oxford, South Parks Road, Oxford OX1 3QU, UK, [b]Departamento de Medicina Molecular y Bioprocesos, Instituto de Biotecnología, UNAM. Av. Universidad 2001, CP 62210 Cuernavaca, Morelos, Mexico, and [c]Notre Dame Radiation Laboratory, University of Notre Dame, IN 46556, USA.
E-mail: elspeth.garman@bioch.ox.ac.uk

The rate of radiation damage to macromolecular crystals at both room temperature and 100 K has previously been shown to be reduced by the use of certain radical scavengers. Here the effects of sodium nitrate, an electron scavenger, are investigated at 100 K. For sodium nitrate at a concentration of 0.5 *M* in chicken egg-white lysozyme crystals, the dose tolerance is increased by a factor of two as judged from the global damage parameters, and no specific structural damage to the disulfide bonds is seen until the dose is greatly in excess (more than a factor of five) of the value at which damage appears in electron density maps derived from a scavenger-free crystal. In the electron density maps, ordered nitrate ions adjacent to the disulfide bonds are seen to lose an O atom, and appear to protect the disulfide bonds. In addition, results reinforcing previous reports on the effectiveness of ascorbate are presented. The mechanisms of action of both scavengers in the crystalline environment are elucidated.

Keywords: radiation damage; dose tolerance; radicals; scavengers; sodium nitrate; sodium ascorbate.

1. Introduction

Radiation damage to protein crystals irradiated with X-rays during diffraction experiments is unavoidable. The effects produced and the processes underlying this radiation damage have been reviewed previously (Nave & Garman, 2005; Garman, 2010). The high solvent content of protein crystals, between 20 and 80%, can play a very significant role in damage progression. The interaction between ionizing radiation and solvent causes solvent radiolysis; releasing radicals that react, both locally and at 'long' distance after migration, with moieties in the protein causing changes in structure, some of which are readily detectable in electron density maps. Next to the growth of a suitable crystalline sample, radiation damage is the most significant challenge in both X-ray and electron diffraction for crystallography. It reduces the useful total beam exposure time, often resulting in incomplete and/or lower-resolution data and thus can cause the loss of key structural information.

A major advance in attempts to reduce radiation damage in macromolecular crystallography came with the introduction of cryocooling techniques (Hope, 1988; Garman & Schneider, 1997; Rodgers, 1997; Garman, 1999), the success of which is based on the fact that the diffusion of radicals produced in the surrounding environment is significantly diminished at lower temperatures. It is now known that cooling protein crystals to 100 K gives an increase of around 70-fold in dose (energy deposited/unit mass) tolerance when compared with crystals irradiated at room temperature (RT) (Nave & Garman, 2005). At RT, an inverse dose rate effect has been observed for which the dose tolerance of chicken egg-white lysozyme crystals was greater by a factor of four as the dose rate was increased from 6 Gy s^{-1} to 10 Gy s^{-1} (Southworth-Davies *et al.*, 2007), whereas, at 100 K, damage rates (at the current flux densities used) appear to exhibit no strong dependence on dose rate (Sliz *et al.*, 2003; Leiros *et al.*, 2006; Owen *et al.*, 2006). Electrons (Rao *et al.*, 1983) and also, perhaps, positive holes (absence of an electron) formed in the protein (Jones *et al.*, 1987) are able to migrate even at 100 K, causing both global and specific structural damage that can mislead the biological interpretation of solved structures. The effects of radiation damage can also prevent structure determination by compromising intensity information used in phasing methods, owing to creeping non-isomorphism as the experiment proceeds (Ravelli & Garman, 2006). As the dose increases, the crystal suffers unit-cell expansion, and rotation of the mole-

cules in the unit cell as well as specific structural changes to particular amino acids (Weik *et al.*, 2000; Burmeister, 2000; Ravelli & McSweeney, 2000).

In X-ray diffraction experiments conducted on crystals held at 100 K, global radiation damage is experimentally observed mainly as a decay of the highest-resolution reflection intensities, an increase in scaling *B*-factors and changes in the unit-cell volume (almost always an expansion) (Murray & Garman, 2002; Ravelli *et al.*, 2002). Also, at the electron density level, specific radiation damage is observed. Bond breakage is detected in a reproducible 'pecking order' as the absorbed dose increases. For metal-free protein crystals this is cleavage of disulfide bonds, decarboxylation of aspartic and glutamic acids, OH scission from tyrosines and the breakage of the C—S bond in methionines (Weik *et al.*, 2000; Burmeister, 2000; Ravelli & McSweeney, 2000). The order of rupture within a specific category varies reproducibly with residue environment, although the parameters that govern this order are not yet well characterized (Fioravanti *et al.*, 2007). However, in proteins containing metals, the metal ions are even more susceptible than amino acid residues: at doses considerably lower than the experimental limit of 30 MGy (Gy = J kg^{-1}), a value that reduces the global diffracted intensity to 0.7 or less of its initial value (Owen *et al.*, 2006), metals are often observed to be damaged. Metal centres are particularly swiftly reduced if they are redox active (Yano *et al.*, 2005; Carugo & Carugo, 2005; Macedo *et al.*, 2009; Corbett *et al.*, 2007). Another consequence of radiation damage is a dose-dependent decrease in the occupancies observed for heavier elements: selenium (Rice *et al.*, 2000), bromine (Oliéric *et al.*, 2007), mercury (Ramagopal *et al.*, 2005) and iodine (Evans *et al.*, 2003).

Following the widespread adoption of cryotemperature data collection, several investigations have sought to find methods to further mitigate radiation damage in macromolecular crystallography by the use of radical scavengers. However, in order to design appropriate strategies, it is vital that we obtain an understanding of the chemical basis of radiation damage occurring during X-ray irradiation.

The first studies on protein crystals that made use of radical scavengers to alleviate radiation damage at RT involved soaking 1.2, 2.0 and 30 m*M* styrene into immunoglobin crystals and monitoring two different reflections. The most effective concentration was 2 m*M*, and resulted in a resolution increase from 5.5 Å to 4 Å coupled with a tenfold increase in crystal lifetime (Zaloga & Sarma, 1974; Sarma & Zaloga, 1975). The intensity of the observed diffraction data was increased by the presence of styrene.

Subsequently, Cascio and co-workers (Cascio *et al.*, 1984) substituted water in the mother liquor of crystals from different proteins (α-amylase, canavalin and fructose-1,6-diphosphatase) with 10–20% (*w*/*v*) polyethylene glycol of molecular weight 4000–20000 g mol^{-1}. A decrease in the radiation damage was observed for all systems tested. In the most dramatic example, reflections that suffered an intensity reduction of 90% after 20 h exposure to 8 keV X-rays survived for 90 h in the X-ray beam upon addition of 12% PEG 20000 g mol^{-1}, showing less than 10% decay in the diffraction intensity. In a more recent study it was found that radical scavengers have the potential to increase the tolerance of protein crystals to X-ray radiation at RT by a factor of as much as nine at a constant dose rate (Barker *et al.*, 2009). Barker *et al.* (2009) observed a differential effect for solvated electron (e_s^-) and hydroxyl radical ($^\bullet$OH) scavengers. 1,4-Benzoquinone, which interacts preferentially with electrons, was found to be considerably more effective than ascorbate, which interacts preferentially with $^\bullet$OH radicals. The rate constants for these two scavengers in aqueous solution are: 1,4-benzoquinone, $k(e_{aq}^-) = 1.2 \times 10^{10}\ M^{-1}\ s^{-1}$ (Buxton *et al.*, 1988) and $k(^\bullet\text{OH}) = 1.2 \times 10^{9}\ M^{-1}\ s^{-1}$ (Milosavljević & Mićić, 1978); ascorbate, $k(e_{aq}^-) = 3 \times 10^{8}\ M^{-1}\ s^{-1}$ (Buxton *et al.*, 1988) and $k(^\bullet\text{OH}) = 8 \times 10^{9}\ M^{-1}\ s^{-1}$ (Schuler *et al.*, 1974). It should be noted that these rates were measured in irradiated aqueous solutions with low concentrations of scavenger (m*M*). Buxton *et al.* (1988) have provided a useful compilation of key rates relevant to these scavenger studies. Importantly, at RT the addition of either of these scavengers changed the form of the decay of the diffraction intensity with dose from first order to zeroth order. As mentioned above, a dose-rate effect has also been reported at RT: crystals irradiated at a higher dose rate appear to have a greater dose tolerance, so any RT studies of the comparative efficacy of scavengers must be carefully conducted at the same dose rate for crystals with and without scavengers.

At cryotemperatures (100 K) the effectiveness of radical scavengers is still a matter of debate. Murray & Garman (2002) studied the effects of styrene and ascorbate as scavengers at cryotemperatures (Murray & Garman, 2002). By analysing the rate of diffraction intensity decay of HEWL crystals, they observed less susceptibility to radiation in crystals grown with 0.5 *M* ascorbate, as shown from analysis of specific structural damage to disulfide bonds in electron density maps and from the much lower values of refined atomic *B*-factors obtained from the ascorbate co-crystallized HEWL (Ravelli & Garman, 2006). No improvement in these parameters was observed for styrene, and, because of its toxicity, no further investigations with it have been undertaken. Also, with the ascorbate co-crystals, by using an offline microspectrophotometer (Bourgeois *et al.*, 2002), Murray & Garman (2002) observed the quenching of a 400 nm peak which developed in the native samples. The 400 nm peak has been attributed to a disulfide radical anion (Armstrong, 1990; Weik *et al.*, 2002).

Additionally, nicotinic acid and 5,5′-dithiobis-2-nitrobenzoic acid (DTNB) have been found to mitigate particular manifestations of radiation damage when used on crystals of HEWL, thaumatin and elastase at 100 K (Kauffmann *et al.*, 2006). Nicotinic acid protected disulfides from damage, but not acidic residues in HEWL and elastase. However, for DTNB the opposite result was found (disulfides were not protected although aspartates were), suggesting that different mechanisms were at work. Recently the above results have been called into question by results from measurements of the decay *R*-factor (see below) of four native and four nicotinic-

acid-soaked trypsin crystals, where no statistically significant difference in susceptibility was found between the two groups (Nowak *et al.*, 2009).

To develop a signature for effective scavengers for specific radiation damage, the disulfide radical anion 400 nm peak was studied (Southworth-Davies & Garman, 2007) with an online microspectrophotometer (McGeehan *et al.*, 2009). Cryoprotected 0.1 *M* disulfide test systems held at 100 K, with and without potential scavengers, were subjected to X-ray radiation. In order to model thiol (SH) and disulfide (SS) groups, the experiments used cysteine (SH), cystine (SS) and oxidized α-lipoic acid (SS). Ascorbate at concentrations between 0.3 *M* and 1 *M* quenched the appearance of the 400 nm peak for the tested disulfide systems. On the other hand, TEMP (2,2,6,6,-tetramethyl-4-piperidone), while effective on oxidized α-lipoic acid, was unable to quench the damage to cystine. 1,4-Benzoquinone was effective on both disulfide test systems, at concentrations higher than 0.4 *M*.

As part of a wider study on the experimental parameters affecting rates of radiation damage, Borek *et al.* (2007) investigated monoclinic lysozyme crystals grown with nitrate in the mother liquor, comparing their behaviour with that of tetragonal lysozyme crystals grown in sodium chloride plus sodium acetate. For the former, the electron density maps showed changes around ordered nitrates following irradiation, but almost no loss of density around disulfide bridges, whereas in the latter case disulfide bond breakage was observed (Borek *et al.*, 2007). In later work by Holton (2007), 1 *M* nitric acid and 0.8 *M* ascorbate were added separately to 0.25 m*M* SeMet solutions, which were then irradiated at 110 K while their XANES spectra were monitored. 'Protection factors' of $48 \pm 9\%$ and $110 \pm 9\%$, respectively, were obtained for these scavengers. The term 'protection factor' was used to compare pairs of $D_{1/2}$ measurements ($D_{1/2}$ being the dose at which half of the SeMet had been damaged) and computed as the absolute difference between two $D_{1/2}$ measurements divided by the smaller of the two $D_{1/2}$ values (Holton, 2007).

For crystals of iron- and copper-containing metalloproteins, potassium hexacyanoferrate(III) was found to be the only molecule investigated which was capable of mitigating photoreduction rates (Macedo *et al.*, 2009). Changes in the UV-visible spectra, measured with an online microspectrophotometer, were used to follow photoreduction of the redox active metal ions. After analysing the behaviour of general radiation damage indicators [unit-cell volume change, $R_{\rm meas}$, $I/\sigma(I)$, completeness in the highest-resolution shell and Wilson *B*-factors], the authors confirmed ascorbate as an efficient scavenger protecting against global and certain specific radiation damage but not useful for preventing metal centre reduction. Macedo *et al.* (2009) also suggested HEPES [4-(2-hydroxyethyl)-1-piperazineethanesulfonic acid] and 2,3-dichloro-1,4-naphthoquinone as potential scavengers.

The motivation of the work reported here was to extend the combined results summarized above and to separate the effects of electron and $^{\bullet}$OH scavenging to assist in rationalizing the relative efficacy of different scavengers. To this end, nitrate, solely an electron (e^-) scavenger, $k(e^-_{aq}) = 9.7 \times 10^9\ M^{-1}\ s^{-1}$ (Buxton *et al.*, 1988), was chosen, and its effects investigated at 100 K both by microspectrophotometry on solutions and by a study of soaked lysozyme crystals. It should also be noted that, in RT aqueous solutions, high concentrations of nitrate can also scavenge electrons before they are solvated (Hiroki *et al.*, 2002). Some additional results on the use of ascorbate as a scavenger at 100 K (Murray & Garman, 2002; Southworth-Davies & Garman, 2007; Holton, 2009) are also presented.

2. Materials and methods

2.1. Protein crystallization

Chicken egg-white lysozyme (HEWL) crystals were grown by mixing 4 + 4 µl drops of 50 mg ml^{-1} protein solution in 200 m*M* sodium acetate buffer at pH 4.7 with precipitant consisting of 200 m*M* sodium acetate buffer at pH 4.7 containing 10% *w*/*v* NaCl. Crystals grew in space group $P4_32_12$ with cell dimensions $a = b = 77.78$ Å, $c = 38.45$ Å, and $\alpha = \beta = \gamma = 90.0^\circ$, and a solvent content of 38%. Cryosolutions were prepared by replacing water in the original precipitating solution by 30% glycerol (*v*/*v*), and crystals were soaked in this for 1 min. Ascorbate HEWL co-crystals were grown by replacing water in the precipitant solution by 1.0 *M* sodium ascorbate. Nitrate HEWL crystals were prepared by soaking two different groups of native crystals for 4 and 8 min, respectively, in the cryosolution described above but replacing some of the water by sodium nitrate to give a final concentration of 0.5 *M*.

Diffraction data were collected from five crystals: a native sample (designated 'nat') grown as described above, one co-crystallized with ascorbate (designated 'asc') and three soaked in sodium nitrate, two of which were soaked for 4 min (designated 'nitrate I4' and 'nitrate II4') and the other for 8 min (designated 'nitrate III8'). Crystal dimensions were 50 × 40 × 25 µm for 'nat', 60 × 50 × 20 µm for 'asc', 50 × 50 × 25 µm for 'nitrate I4', 55 × 50 × 30 µm for 'nitrate II4' and 60 × 40 × 30 µm for 'nitrate III8'.

2.2. Online UV-visible microspectrophotometry

Absorption spectra from solutions and crystals were collected on beamline ID14-4 (McCarthy *et al.*, 2009) at the ESRF using an online microspectophotometer, arranged and operated as described elsewhere (McGeehan *et al.*, 2009). Spectra were collected from a cryocooled protein solution held in a rayon cryoloop at 100 K containing a solution composed of 35 mg ml^{-1} HEWL lysozyme and 30% glycerol in 100 m*M* pH 4.7 sodium acetate buffer using the same methods as detailed by Southworth-Davies & Garman (2007). Data were also recorded from a 35 mg ml^{-1} HEWL nitrate solution containing 0.5 *M* sodium nitrate, 30% glycerol in 100 m*M* pH 4.7 sodium acetate buffer. The best loop orientation was determined in order to maximize the 280 nm absorption peak that originates from aromatic protein residues. All spectra were recorded using the *OOIBase32* software (Ocean Optics). Each spectrum consisted of 2048

absorbance points within the wavelength range 200–1100 nm. Scans were recorded every 307 ms for 4 min 20 s. Data recording started 20 s before the sample was subjected to thirty 1 s X-ray irradiations, with around 3 s (corresponding to the detector readout time) between each exposure to give a total of 120 s, followed by a 120 s spectra collection period with the beam off (20 + 120 + 120 = 260 s total). The loop containing the protein solution was incrementally rotated by $\Delta\varphi = 1^\circ$ during each X-ray irradiation period (total $\Delta\varphi = 30^\circ$). Spectral data recorded at $\varphi = 0^\circ$ before the X-ray exposure were used to establish a stabilized blank. The incident X-ray beam, of size 50 µm × 100 µm and wavelength $\lambda = 0.939$ Å (energy 12.7 keV), was used at 100% transmission. In order to process and merge all individual scans, a Perl script was written to obtain plots such as those in Fig. 1.

Table 1
Data collection parameters.

All five crystals initially diffracted to beyond the detector edge (1.7 Å).

	Native	Ascorbate	Nitrate I4	Nitrate II4	Nitrate III8
Crystal dimensions (µm)	50 × 40 × 25	60 × 50 × 20	50 × 50 × 25	55 × 50 × 30	60 × 40 × 30
Dose rate (kGy s^{-1})	15.6	26.3	30.0	26.8	8.6

2.3. Data collection and processing

Diffraction data collection also took place at ESRF beamline 14-4 at an X-ray wavelength of 0.939 Å, using an Oxford Cryosystems 700 series cryostream and an ADSC Q315r mosaic CCD detector (ADSC, Poway, CA, USA). The crystal sizes were chosen in order to match the beam size: this ensured a uniform dose for all crystal regions. The crystal-to-detector distance was fixed at 267.74 mm for all data collections, and all five crystals initially diffracted to the edge of the detector (1.7 Å). The same strategy as used previously to measure the experimental dose limit (Owen *et al.*, 2006) was employed for each lysozyme crystal. Briefly, on each crystal at least six complete data sets (*d*1–*d*6) of 90 images were collected (Table 1) without translating the crystal in between data sets, with an oscillation angle per image ($\Delta\varphi$) of 1° and an exposure time of 2 s each using a beam transmission of 10.5%. In between each dataset the crystal was subjected to a 'burn' at 100% beam transmission during which nine images each of $\Delta\varphi = 10^\circ$ with an exposure time of 6 s per image were recorded. Dose rates were in the range 9–30 kGy s^{-1} (see Table 1) and the starting φ-values were chosen in order to irradiate the same section of the crystal as had been exposed for the datasets each time.

Two parallel methods were utilized to process the data. First, integration was undertaken using the program *MOSFLM* (Leslie, 2006). Integrated reflections were then sorted, truncated and scaled with *SORT*, *TRUNCATE* and *SCALA*, respectively (Evans, 2006). Using Protein Data Bank code 2W1L (Cianci *et al.*, 2008) as the model, the first six data sets (*d*1–*d*6) (except for 'nitrate I4' where only five data sets could be refined) collected from each crystal were refined independently by rigid-body minimization and subsequent restrained refinement, both operations being carried out with *REFMAC* (Murshudov *et al.*, 1999). Molecular replacement of the 2W1L model into the data was unnecessary, since 2W1L was determined from crystals in the same space group and unit cell as the crystals used here. The above programs are all contained in the CCP4 suite (Collaborative Computational Project, Number 4, 1994). Finally, *COOT* (Emsley *et al.*, 2010) was used for water molecule addition and manual model building. Models for all the datasets were refined to a resolution of 2.0 Å, at which the values of $I/\sigma(I)$ and $R_{\rm merge}$ were still reasonable for the highest-dose dataset. Refinement was continued until the R values were less than 0.20 and $R_{\rm free} < 0.25$. Alternatively, data were integrated and scaled with *XDS* and *XSCALE*, respectively (Kabsch, 2010). The decay R-factor ($R_{\rm d}$), which is the difference in the observed intensity of the unique reflections *hkl* detected on frames separated by a dose difference of ΔD, was then calculated using *XDSSTAT* (Diederichs, 2006). The values I/I_0 [mean intensity ($I_{\rm mean}$) for the dataset divided by $I_{\rm mean}$ of the first] for each dataset for the resolution range 35.0–1.8 Å was extracted from both *SCALA* (Evans, 2006) and *XSCALE* (Kabsch, 2010).

Fourier difference maps were calculated as described by Barker *et al.* (2009). Briefly, for each crystal, the structure factor amplitudes and phases from the final model of the first data set (*d*1) were used, and these same phases and the structure factor amplitudes of the remaining data sets in a series (*d*2–*d*6) were combined using the CCP4 utility software program *CAD*. *FFT* was then used to produce Fourier difference maps $F_{0dx} - F_{0d1}$ (where *dx* is any data set other than the first).

2.4. Dose calculations

Dose calculation was carried out using *RADDOSE* version 2 (Paithankar *et al.*, 2009; Murray *et al.*, 2004). In order to compute the dose, the program requires the values of the beam parameters (including the energy, profile, size/area and flux) and crystal properties (unit cell, space group, number of molecules per asymmetric unit, composition, size and thickness). From these parameters *RADDOSE* calculates the absorption coefficient of the sample using an average amino acid residue composition of 5C + 1.35N + 1.5O + 8H atoms. In *RADDOSE* the absorbed dose is obtained by estimating the energy deposited in the crystal by the incident X-ray beam as a consequence of the photoelectric effect. The beam flux in photons s^{-1} was obtained by using a 500 µm Hamamatsu diode to calibrate the in-line beam intensity monitor which is composed of a kapton foil mounted at 45° to the X-ray beam and an associated silicon pin diode mounted above it: this procedure has been described in detail previously (Owen *et al.*, 2009).

The size of the crystal was measured by using the in-line microscope integrated into beamline ID14-4. A 360° rotation

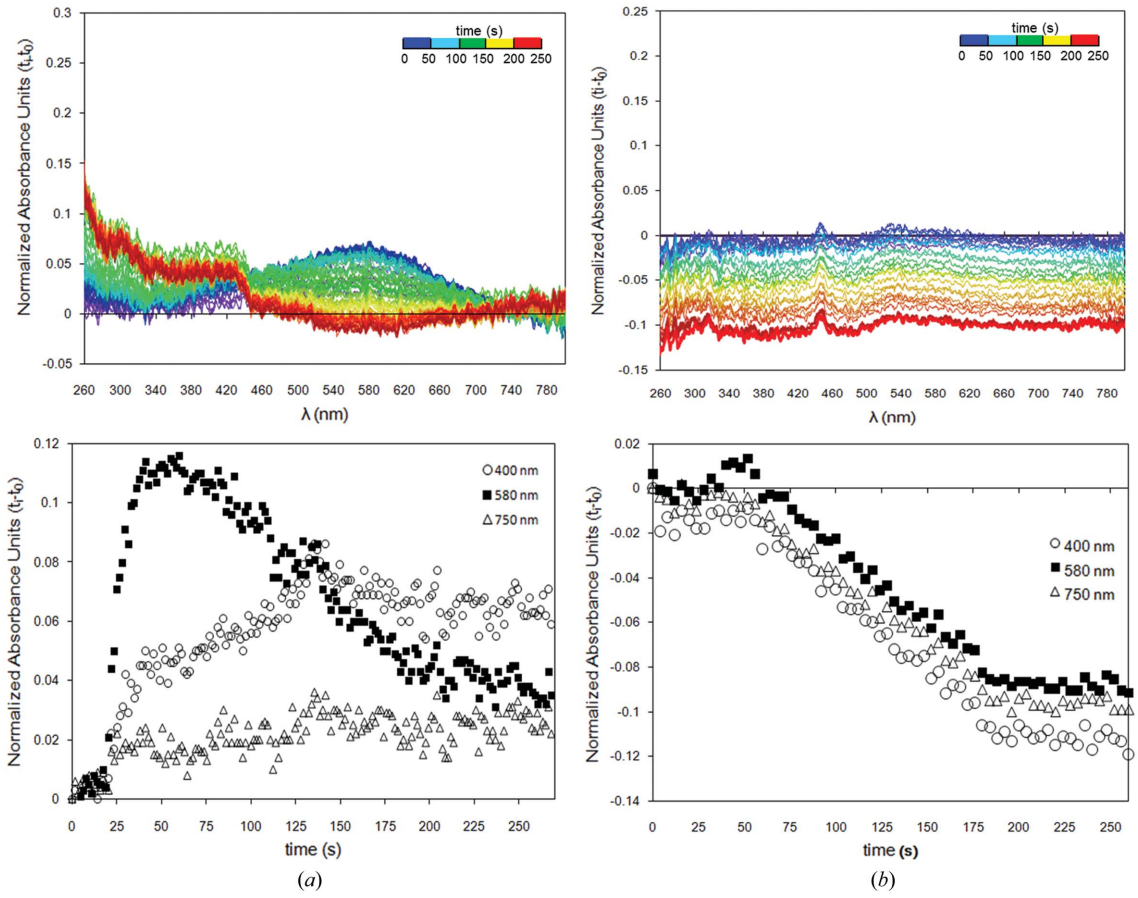

Figure 1
Time-dependent UV-visible spectra (upper panels) and changes in absorption at 400, 580 and 750 nm (lower panels) collected from a lysozyme solution (*a*) without and (*b*) with nitrate. The maxima observed at 400 and 580 nm in the solution without nitrate [(*a*), upper panel] correspond to the formation of the disulfide radical anion and solvated electrons, respectively, both of which are quenched by the presence of nitrate [(*b*), upper panel]. Absorption at 750 nm represents the background signal.

of the crystal around the φ axis allowed an estimation to be made of all three dimensions of the irradiated crystals. A beam size of 50 × 100 µm was chosen in order to obtain a Gaussian profile.

3. Results

3.1. Microspectrophotometry

During the X-ray exposure of the lysozyme solution with glycerol at 100 K, an absorption peak grew at 580 nm, readily attributable to solvated electrons. This peak appeared during the first milliseconds of irradiation, increased until the end of the 1 s exposure, decayed a small amount during the readout time, and then increased again during the next beam exposure, giving a 'saw tooth' appearance to the absorption. However, after eight exposures the intensity of the 580 nm absorption peak reached a maximum and on subsequent irradiations its magnitude decreased. In concert with the solvated electron formation, an absorption peak at ∼400 nm appeared. This signal corresponds to the formation of the disulfide radical anion, RS-SR′$^{\bullet-}$ (Weik *et al.*, 2002). The decrease after the eighth exposure which was observed in the 580 nm peak ascribed to the solvated electrons was accompanied by a steady increase in the absorption at 400 nm attributed to the disulfide radical anions (see Fig. 1*a*). It is thus tempting to postulate that a fraction of the solvated electrons reacted with the remaining intact disulfide bridges in the protein. Following the last X-ray exposure, both absorption peaks decayed away, but the 400 nm peak lifetime was longer than that of the solvated electrons at 580 nm (Fig. 1*a*).

In order to probe the effectiveness of nitrate as an electron scavenger in the same lysozyme solution, UV-visible spectra were recorded from a HEWL protein solution with sodium nitrate added (final concentration 0.5 *M*) while it was irradiated by the X-ray beam. As can be seen in Fig. 1(*b*), neither 400 nm nor 580 nm peaks were observed in nitrate-containing HEWL solutions. The overall decrease in absorption observed in these spectra is a consequence of the rotation of the sample in the beam, which results in a change in the optical path length; in this case a decrease because of the difference in the relative thickness of the sample as seen by the microspectrophotometer at the beginning (thicker sample) and end (thinner sample) of the φ rotation range. Since ascorbate has previously been found by offline and online microspectrophotometry to quench the 400 nm disulfide anion

absorption peak at 100 K (Southworth-Davies & Garman, 2007; Murray & Garman, 2002), measurements on it were not repeated.

3.2. Diffraction

Following analysis and scaling of the diffraction images for all the datasets using both *SCALA* and *XSCALE*, the plots of the mean I/I_0 for each dataset against dose by fitting straight lines to the intensity decay data for the five different crystals were inspected and the dose to half intensity values ($D_{1/2}$) extracted. Small differences in calculated $D_{1/2}$ values were observed depending on the software used to calculate the mean I/I_0 [*SCALA* or *XSCALE*; see Figs. 2(*a*) and 2(*b*)]. However, irrespective of the software employed, the differences between crystals detailed below were maintained. The results from *SCALA* and *XSCALE* are shown with those from *XSCALE* in brackets in the following. For the 'nat' lysozyme crystal, $D_{1/2}$ was 12.5 MGy (12.9 MGy), in agreement within experimental error with Teng & Moffat and with Southworth-Davies who reported values of $D_{1/2}$ to be around 10 MGy (Teng & Moffat, 2000, 2002; Davies, 2008) for lysozyme. This value is approximately four times smaller than the $D_{1/2}$ of 43 MGy determined by us previously for holo and apoferritin (Owen *et al.*, 2006). Thus lysozyme crystals appear to have a higher innate sensitivity to X-ray radiation than those of ferritin. This is in contrast to the results reported by Kmetko *et al.* (2006), who gave coefficient of sensitivity (S_{AD}, slope of plot of B_{rel} *versus* dose) values of 0.012 Å^2 MGy^{-1} for lysozyme and 0.018 Å^2 MGy^{-1} for ferritin. For the lysozyme 'nat' data reported here the corresponding value of S_{AD} is 0.010 Å^2 MGy^{-1}, which agrees with Kmetko *et al.* within experimental error and is significantly higher than the values estimated for the scavenger-containing crystals. Clearly there is a discrepancy amongst these findings concerning the relative radiation sensitivity of ferritin crystals.

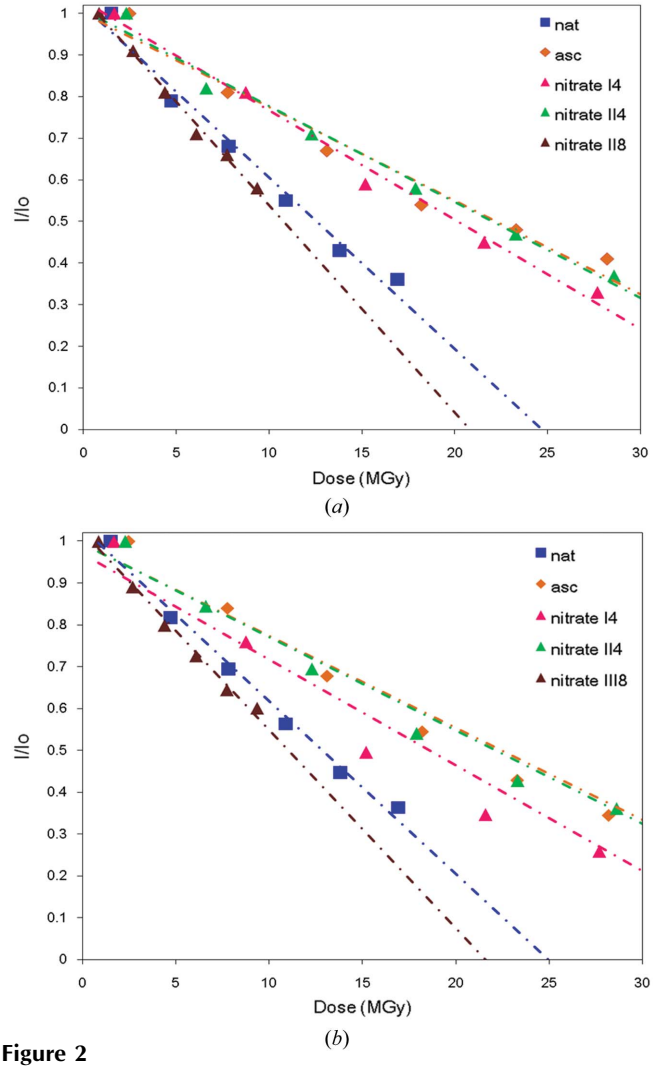

Figure 2
Comparison of the overall intensity decay between native ('nat'), co-crystallized ascorbate ('asc') and nitrate-soaked crystals ('nitrate I4', 'nitrate II4' and 'nitrate III8') from HEWL. Mean normalized intensity, I/I_0 (summed between resolution bins of 35 Å and 1.8 Å), per dataset *versus* dose plots showing the overall intensities calculated from (*a*) *SCALA* and (*b*) *XDS/XSCALE*. The lines are linear fits to the decay.

Both ascorbate and nitrate increased $D_{1/2}$ almost twofold, with $D_{1/2}$ = 22.0 MGy (22.4 MGy) for 'nitrate II4' and $D_{1/2}$ = 22.2 MGy (22.4 MGy) for the 'asc' crystal. For the 'nitrate I4' crystal a value of $D_{1/2}$ = 19.1 MGy (18.8 MGy) was obtained but a lower $D_{1/2}$ of 10.8 MGy (11.1 MGy) was observed for the 8 min nitrate-soaked crystal 'nitrate III8'. This $D_{1/2}$ is even lower than that observed for the native crystal, suggesting that the longer soaking period was detrimental to the crystal dose tolerance. As indicated by the smaller $D_{1/2}$, the resolution loss occurred at a lower dose in the native crystal than in 'nitrate II4' and 'asc' (Fig. 3*a*).

Although, as expected, the overall unit-cell volume of each crystal increased with dose, analysis of the unit-cell parameters showed differences in this increase in the nitrate crystals (Fig. 3*b*). The 'nitrate I4' crystal showed the fastest expansion in unit-cell volume: a 2% expansion before a dose of 10 MGy was reached. Additionally, and in contrast to the results from the other four crystals where a linear trend was observed, the expansion behaviour of this crystal was somewhat erratic. The 'nitrate III8' crystal showed a faster linear unit-cell expansion than the 'nat', 'asc' and 'nitrate II4'. Unit-cell expansion in the 'nat', 'asc' and 'nitrate II4' behaved in a very similar way, *i.e.* a linear trend with an approximate rate of 2% per 25 MGy. However, the variation reported here is not surprising, as it has already been established that the increase in unit-cell volume with dose is not systematically the same for crystals of the same protein and habit under the same conditions (Murray & Garman, 2002; Ravelli *et al.*, 2002).

3.3. Decay *R*-factor

The efficiency of scavengers was also compared by calculating the decay *R*-factor (R_d) (Diederichs, 2006). In this method the intensity of the same reflection *hkl* from different images (*i.e.* collected after a different dose) is compared. Thus, intensities from all reflections on the first image from the first dataset collected at the lowest dose are compared with intensities from equivalent reflections from images taken after exposure to higher doses. Consistent with the $D_{1/2}$ results

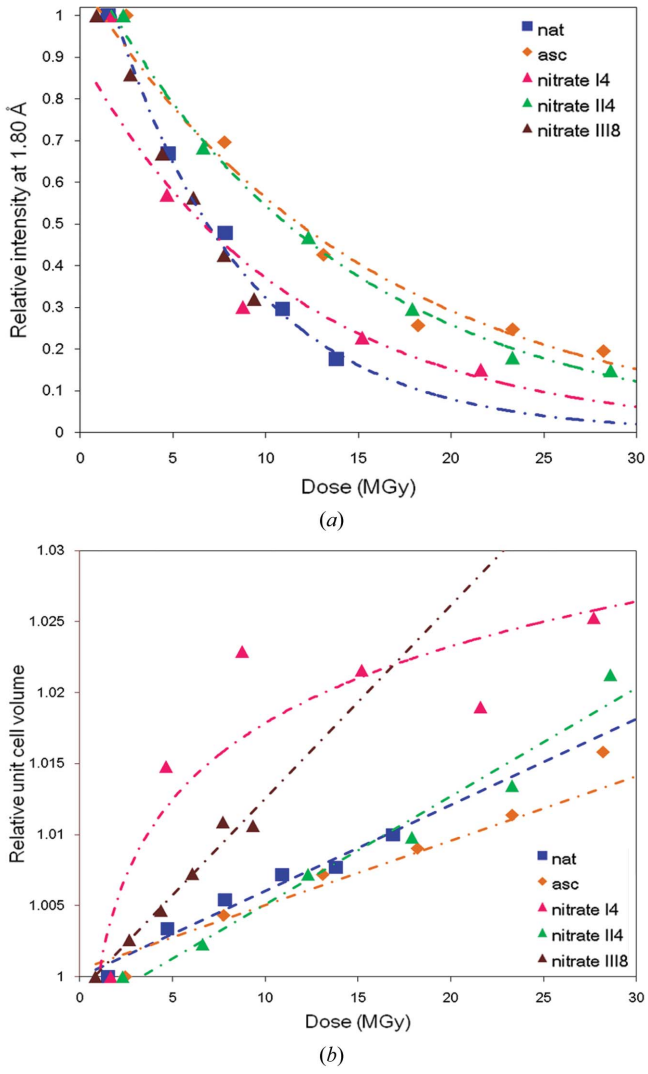

Figure 3
(*a*) The relative intensity loss of the highest-resolution shell (1.90–1.80 Å) fitted with exponential functions (*b*) and unit-cell volume changes observed in native ('nat'), ascorbate co-crystallized ('asc') and nitrate-soaked crystals ('nitrate I4', 'nitrate II4' and nitrate III8) from HEWL.

mentioned above, 'asc' and 'nitrate II4' showed significantly decreased $R_{\rm d}$ values, implying a substantial increase in tolerance to radiation damage. However, different results than were indicated by the $D_{1/2}$ analysis were obtained for 'nitrate III8' and 'nitrate I4' crystals (Fig. 4). While $R_{\rm d}$ indicated a faster decay for 'nitrate I4' than for the native HEWL crystal, the opposite was observed for 'nitrate III8', where slower decay was observed. The only difference between the three nitrate-soaked crystals was the soaking time and the dose rate. Owing to flux fluctuations during the data collection period, the 'nitrate I4' crystal was exposed to a higher dose-rate regime compared with the remaining four crystals tested (Table 2). A dose-rate effect cannot be ruled out from our results, although thus far only small dose-rate effects on global and specific damage rates at 100 K have been reported at the flux densities currently in use at third-generation synchrotrons (Owen *et al.*, 2006; Leiros *et al.*, 2006).

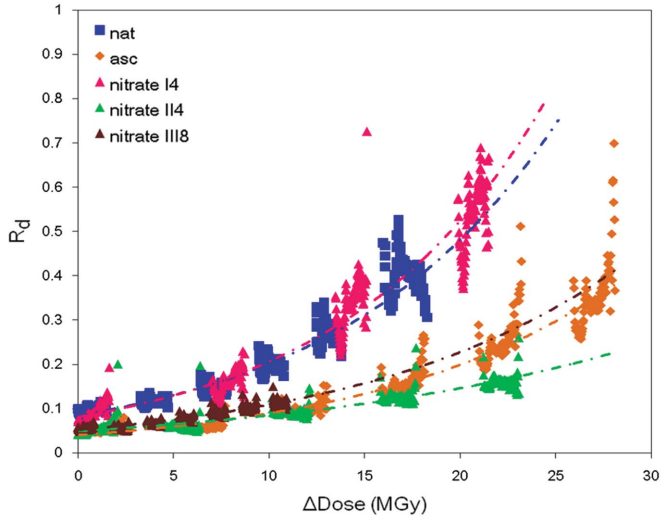

Figure 4
Decay factor ($R_{\rm d}$) analysis of the intensities from native ('nat'), ascorbate ('asc') and nitrate crystal ('nitrate I4', 'nitrate II4' and 'nitrate III8') scavenger datasets.

3.4. Specific damage

Inspection of the electron density of the most susceptible amino acids (cysteines forming S—S bonds, aspartic and glutamic acids, tyrosines and methionines) demonstrated that both scavengers diminish the damage to residues, but interesting differences were observed. Ascorbate increased the dose tolerance of the Cys6—Cys127 disulfide bond by a factor of three, as judged by comparing the electron density in Fourier difference maps at 0.25 e^{-} A^{-3}, since the first damage to Cys6—Cys127 was observed at 4.7 MGy for the native crystal but at 13 MGy for 'asc' [Figs. 5(*a*) and 5(*b*)]. In contrast, the addition of nitrate increased the tolerance by a factor of five in 'nitrate II4', where the damage to disulfide bonds at a dose of 23.3 MGy is about the same as that to the native after a dose of 4.7 MGy. However, ascorbate protects better against the decarboxylation of acidic residues (Asp and Glu) than does nitrate. For example, the decarboxylation of Asp52 is first observed at 8.8 MGy in 'nitrate I4' (data not shown), and for the 'nat' and 'nitrate II4' crystals comparable damage occurs at 7.8 and 12.3 MGy, respectively [see Figs. 6(*a*) and 6(*c*)]. In contrast, specific damage to Asp52 in 'asc' appears after 18.2 MGy (Fig. 6*b*), considerably higher than the value observed for the 'nitrate I4' and 'nitrate II4' crystals. No Asp52 damage was observed in 'nitrate III8' up to the maximum dose of 10.9 MGy (not shown) to which it was subjected. In the case of residue Asp48, decarboxylation is first observed at 16.9 MGy in 'nat', while for 'nitrate II4' damage appears after 23.3 MGy and no damage is observed in the 'asc' crystal even at 28.2 MGy (data not shown). The same differential damage is present in Asp87, being damaged after 10.9 MGy ('nat') and 12.3 MGy ('nitrate II4'), but only by 18.2 MGy in the 'asc' crystal (data not shown).

For the first time, electron density corresponding to a sodium ascorbate molecule was observed in the maps derived from the co-crystallized ascorbate HEWL crystal and was

Table 2
Data processing statistics.

Values for the highest-resolution shell, 1.9–1.8 Å, are shown in parentheses.

Crystal	Dataset	Cumulative dose (MGy)	Unique reflections	Multiplicity	Completeness (%)	$I/\sigma(I)$	R_{merge} (%)	*B* Wilson value (A^2)	I_{Mean} (*SCALA*)	I/I_0 (*SCALA*)
nat	1	1.51	11322	6.9 (7.1)	100.0 (100.0)	5.4 (2.8)	8.6 (26.2)	16.2	1389.9	1.00
	2	4.73	11374	6.9 (7.1)	100.0 (100.0)	4.9 (2.1)	9.4 (34.7)	17.99	1096.4	0.79
	3	7.82	11382	6.9 (7.1)	100.0 (100.0)	4.9 (1.5)	9.6 (48.8)	19.78	946.4	0.68
	4	10.9	11401	6.9 (7.1)	100.0 (100.0)	4.5 (0.9)	11 (80.9)	22.45	770.3	0.55
	5	13.8	11414	6.9 (7.1)	100.0 (100.0)	4.0 (0.5)	13.0 (–)	25.19	602	0.43
	6	16.9	11437	6.9 (7.1)	100.0 (100.0)	3.6 (0.3)	15.6 (–)	27.06	495	0.36
asc	1	2.46	11389	6.8 (7.1)	100.0 (99.9)	7.0 (5.9)	5.6 (11.3)	14.3	13108	1.00
	2	7.76	11454	6.8 (7.1)	100.0 (99.9)	6.6 (4.7)	5.9 (15.2)	16.6	10689	0.81
	3	13.1	11508	6.8 (7.0)	100.0 (99.9)	6.2 (2.4)	7.2 (30.0)	19.3	8807.3	0.67
	4	18.2	11527	6.7 (6.9)	100.0 (100.0)	4.9 (1.0)	10.1 (73.7)	22.1	7034.2	0.54
	5	23.3	11549	6.6 (6.8)	100.0 (100.0)	3.4 (0.4)	15.9 (–)	21.7	6259.7	0.48
	6	28.2	11584	6.5 (6.6)	100.0 (99.9)	2.4 (0.2)	23.7 (–)	22.2	5359.5	0.41
nitrate I4	1	1.68	11132	6.6 (6.7)	98.2 (99.4)	7.1 (3.1)	6.8 (24.0)	15.23	5048.5	1.00
	2	8.76	11251	6.6 (6.7)	98.2 (99.4)	5.9 (1.2)	9.5 (57.2)	18.06	4078.9	0.81
	3	15.2	11334	6.6 (6.7)	98.1 (99.4)	4.0 (0.4)	15.5 (–)	21.49	3000.0	0.59
	4	21.6	11347	6.5 (6.7)	98.1 (99.4)	2.1 (0.2)	27.9 (–)	23.71	2262.9	0.45
	5	27.7	11303	6.4 (6.5)	98.1 (99.2)	1.3 (0.1)	43.8 (–)	23.35	1671.8	0.33
nitrate II4	1	2.31	11392	6.6 (6.4)	99.9 (99.9)	7.4 (6.0)	5.8 (11.6)	15.69	18647.1	1.00
	2	6.62	11449	6.5 (6.4)	99.7 (99.9)	6.5 (4.8)	6.3 (15.3)	17.42	15220.7	0.82
	3	12.3	11497	6.4 (6.3)	99.7 (99.9)	6.7 (3.1)	6.4 (24.3)	19.57	13308.0	0.71
	4	17.9	11534	6.3 (6.2)	99.7 (99.9)	6.1 (1.6)	7.5 (44.9)	22.12	10907.9	0.58
	5	23.3	11584	6.3 (6.0)	99.7 (99.9)	5.3 (0.9)	9.1 (80.8)	24.29	8851.1	0.47
	6	28.6	11437	6.2 (6.0)	99.7 (99.8)	4.6 (0.5)	11.2 (–)	25.51	6905.5	0.37
nitrate III8	1	0.856	11425	6.6 (6.8)	100.0 (100.0)	6.3 (2.9)	7.1 (26.4)	17.24	4967.5	1.00
	2	2.68	11447	6.6 (6.8)	100.0 (100.0)	6.2 (2.6)	7.5 (30.4)	16.97	4541.6	0.91
	3	4.39	11481	6.6 (6.8)	100.0 (100.0)	6.1 (2.2)	7.9 (35.6)	17.58	4004.4	0.81
	4	6.08	11515	6.5 (6.8)	100.0 (100.0)	6.0 (1.8)	7.9 (42.8)	19.12	3614.1	0.71
	5	7.73	11537	6.6 (6.8)	100.0 (100.0)	5.2 (1.3)	9.5 (59.6)	19.32	3285.8	0.66
	6	9.35	11536	6.6 (6.8)	100.0 (100.0)	5.2 (1.1)	9.5 (70.9)	21.62	2867.7	0.58

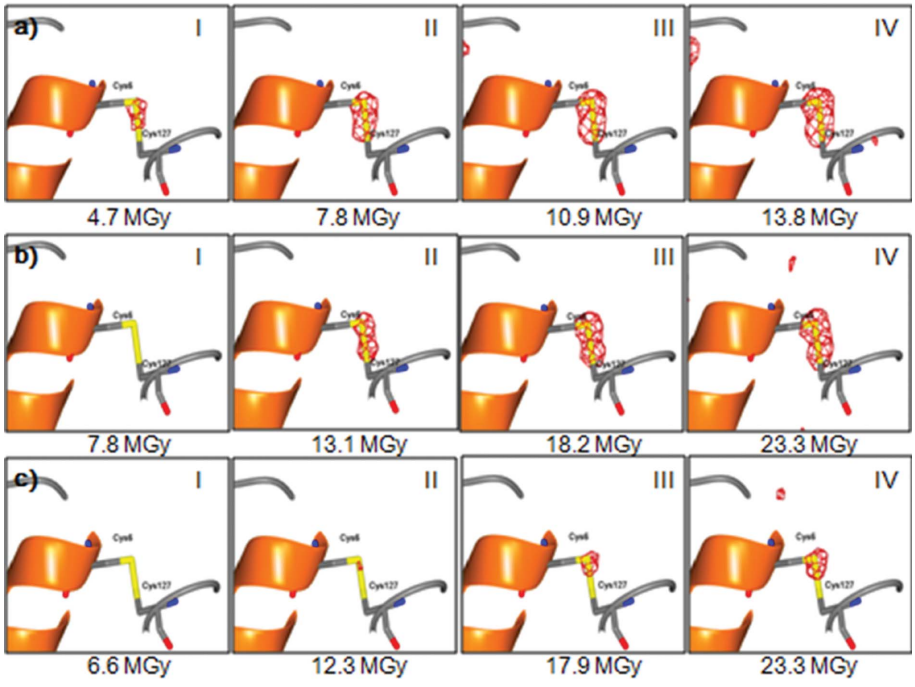

Figure 5
Fourier difference maps showing the varying susceptibility of Cys6—Cys127 disulfide bond breakage in (*a*) 'nat', (*b*) 'asc' and (*c*) 'nitrate II4' crystals as a function of increasing dose (I: *d*2 − *d*1; II: *d*3 − *d*1; III: *d*4 − *d*1; IV: *d*5 − *d*1). The Fourier difference maps (red) are contoured at −0.25 e^- $Å^{-2}$. Note that the absorbed doses for the respective panels in (*a*)–(*c*) are not equal.

observed in all six 'asc' datasets without noticeable radiation decay. The Na atom is coordinated by carbonyl moieties from Ser60, Cys64, Ser72, Arg73 and the O2 from ascorbate (Fig. 7). It is also important to note that two of the four residues coordinating the ascorbate molecule are located in the 69–73 loop that makes crystalline contacts with the same region of a crystallographic neighbouring molecule. Specifically, contacts are made between residues Pro70 and Gly71 from symmetry mates. In contrast to the nitrate reduction with increasing dose (see below), no significant changes are observed in the electron density corresponding to the ascorbate molecule at different doses (not shown).

In $2F_o - F_c$ maps calculated for all nitrate-soaked crystals, four nitrate anions were clearly seen at a σ level of 1.2. Nitrates are located (i) in the structured water shell in the vicinity and at hydrogen-bonding distance from the amide groups of residues Asp68 and Thr69 (not shown), (ii) in the vicinity of the Cys6—Cys127 disulfide bond

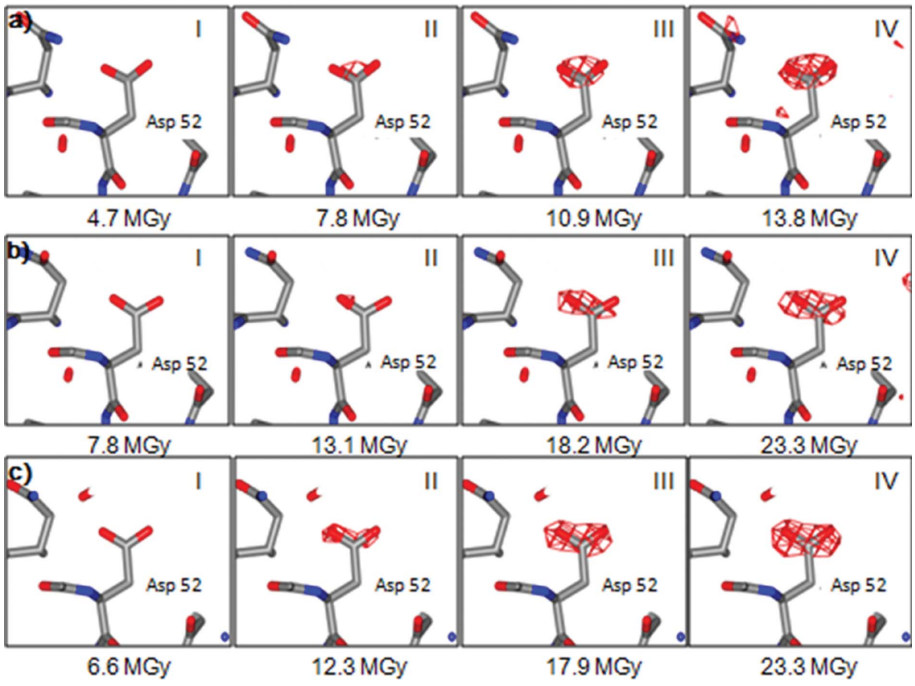

Figure 6
Fourier difference maps showing decarboxylation of Asp52 in (*a*) 'nat', (*b*) 'asc' and (*c*) 'nitrate II4' crystals as a function of increasing dose (I: $d2 - d1$; II: $d3 - d1$; III: $d4 - d1$; IV: $d5 - d1$). The Fourier difference maps (red) are contoured at -0.25 e^{-} Å^{-2}. Note that the absorbed doses for the respective panels in (*a*)–(*c*) are not equal.

(Fig. 8), (iii) within hydrogen-bonding distance of the Ile88 amide group (not shown) and (iv) within hydrogen-bonding distance of Leu25 and Gly26 (not shown). The electron density corresponding to all nitrate anions diminished as the absorbed dose increased. During the reduction of the nitrate anion, shown by the loss of oxygen at a dose of around 6.6 MGy (see Fig. 8*b*), the electron density for the disulfide bond remains intact. At much higher doses (23.3 MGy) the resulting NO_2 disappears (Fig. 8*e*) and, concomitant with this, damage to the disulfide appears in the Fourier difference maps [Fig 5*c*(IV)].

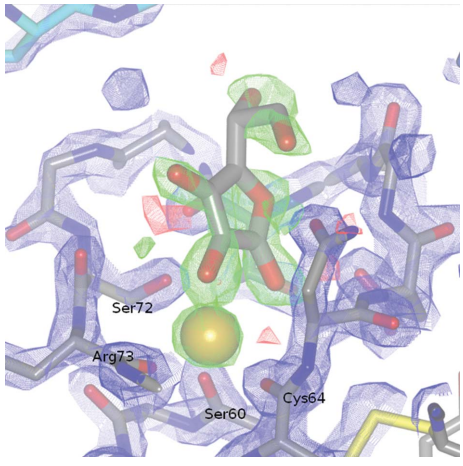

Figure 7
Sodium ascorbate molecule fitted into the calculated electron density from the ascorbate co-crystallized HEWL (*d*1) [$2F_o - F_c$ and $F_o - F_c$ maps at $\sigma = 1.5$ and $\sigma = \pm 3.0$ (green: +; red: −), respectively]. The orange sphere represents a sodium ion.

In agreement with the results detailed above, it has been previously reported that damage on tetragonal HEWL crystals, crystallized from sodium acetate and sodium chloride, was predominantly localized on disulfide bridges, whereas, in the monoclinic form that crystallized from a solution containing sodium nitrate and sodium acetate, damage was concentrated on bound nitrate groups with no peaks present on disulfide bridges up to the doses inflicted (Borek *et al.*, 2007), although no actual dose values are quoted. In addition, Borek *et al.* noted the decarboxylation of acidic residues in the crystals grown in the presence of nitrate (see legend of Fig. 3 in their paper).

4. Discussion

In analysing the effects of various experimental parameters on crystal dose tolerance, it is now clear that the global damage and the specific structural effects have to be considered separately, since it is becoming increasingly apparent from a number of studies that they are not necessarily directly correlated [*e.g.* the reported dependence of specific damage on incident wavelength (Leiros *et al.*, 2006; Homer *et al.*, 2011) whereas there is little evidence of global damage being wavelength dependent (Weiss *et al.*, 2005; Shimizu *et al.*, 2007)]. The results presented above on the addition of scavengers reinforce this observation, as although $D_{1/2}$, a

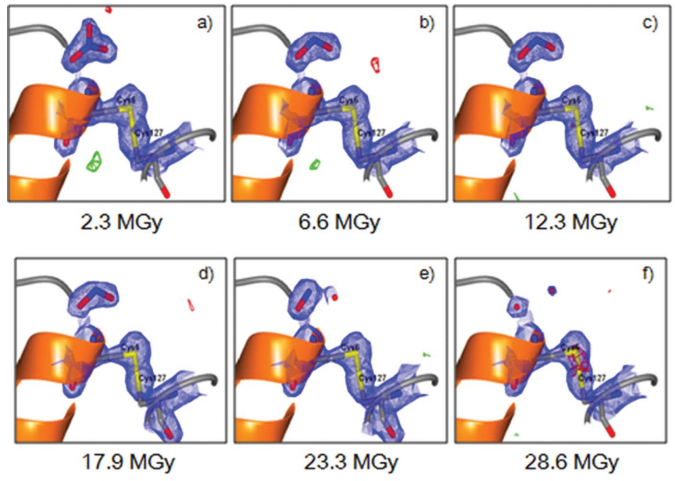

Figure 8
Dose-dependent nitrate reduction observed in the 'nitrate II4'-soaked crystal in the vicinity of the Cys6—Cys127 bond [panels (*a*)–(*f*) correspond to datasets *d*1–*d*6, respectively]. The $2F_o - F_c$ map (blue) is contoured at $\sigma = 1.2$ and the $F_o - F_c$ map is contoured at $\sigma = \pm 3.0$ (green: +; red: −). The reduction of the nitrate molecules correlates with the appearance of density in the difference map of Fig. 5*c*(IV).

metric of global damage, is approximately doubled (from 12.2 MGy to 24.2 MGy) by the addition of nitrate or ascorbate, the effect on the specific damage rate is much larger. There is little S—S bond breakage up to 13 and 23.3 MGy for the addition of ascorbate and nitrate, respectively (compared with 4.7 MGy for the native), and ascorbate also protects the glutamates and aspartates up to 18 MGy compared with the native for which damage to them can be observed at 10.9 MGy. Of particular note when considering the rates of global and specific damage for the nitrate-soaked crystals is the lack of evidence of any damage in the electron density to disulfides even though the mean diffraction intensity decreases significantly.

The mechanism of action of these two scavengers can be postulated as follows. In RT aqueous solution, nitrate is an extremely effective scavenger of excess electrons (Anbar *et al.*, 1967). It reacts exothermically at a near diffusion-limited rate with the fully solvated species, e^-_{aq}, $k(e^-_{aq}) = 9.7 \times 10^9\ M^{-1}\ s^{-1}$ (Buxton *et al.*, 1988), according to the following equation,

$$NO_3^- + e^-_{aq} \rightarrow NO_3^{2-} + H_2O \rightarrow NO_2 + 2OH^-. \qquad (1)$$

Perhaps more significantly, at sufficiently high concentrations, it also intercepts presolvated ('dry') electrons even more efficiently with $k = 10^{13}\ M^{-1}\ s^{-1}$ (Hiroki *et al.*, 2002). In our experiments, performed at cryotemperatures, photoelectrons liberated during X-irradiation of protein crystals induce a cascade of secondary electrons which interact strongly with the environment of the beam path causing further ionizations. Many are trapped in the medium, giving a characteristic broad absorbance band in the visible, typically peaking around 580 nm in cryocooled systems. In the native crystals a thermodynamically favoured path leads to the reduction of disulfide bonds and hence the observed damage shown in Fig. 5(*a*). From the evidence presented above it is clear that nitrate also provides a sink for these radiolytically generated electrons (Fig. 5*c*). In addition, the optical absorption attributed to electrons trapped in the surrounding medium is also seen to be quenched. Nitrate thus effectively mitigates reductive damage. This is particularly clearly seen in Fig. 8, where the disulfide bond retains its crystallographic integrity until 23 MGy, while the adjacently located nitrate is seen to cleave an oxygen. This is the first clear crystallographic demonstration of the chemistry involved in its scavenging action.

Ascorbate, on the other hand, is a powerful antioxidant. Again in solution, ascorbate rapidly scavenges radiolytically produced 'holes' (lack of an electron). In the case of dilute aqueous solution, the initially formed hole, $H_2O^{\bullet+}$, rapidly converts to the hydroxyl radical, $^\bullet OH$, through the reaction

$$H_2O^{\bullet+} + H_2O \rightarrow H_3O^+ + {}^\bullet OH. \qquad (2)$$

The $^\bullet OH$ then reacts with ascorbate at a near-diffusion-limited rate [$k(^\bullet OH) = 8 \times 10^9\ M^{-1}\ s^{-1}$ (Schuler *et al.*, 1974)] according to

$$AH^- + {}^\bullet OH \rightarrow AH^\bullet + OH^- \rightarrow A^{\bullet-} + H_2O. \qquad (3)$$

Unscavenged, the strongly oxidizing hydroxyl radicals can remove electrons from, for example, simple amino acids resulting in their prompt decarboxylation (Hug *et al.*, 2000; Wisniowski *et al.*, 2002).

In addition, at sufficiently high concentrations, ascorbate can presumably donate electrons to competitively fill the initial holes.

In the protein crystal at cryotemperatures, holes created in the vicinity of acid residues will be promptly filled by donation from ascorbate, thus preventing decarboxylation. Again this can be seen from the electron density maps shown in Fig. 6. In the native crystal, decarboxylation occurs readily and damage is already seen at 7.8 MGy, while in the presence of co-crystallized ascorbate no decarboxylation is observed until 18 MGy. In accordance with equation (2) there should be no crystallographic evidence for the consequent oxidation of the ascorbate ion, since the ascorbyl nucleus remains unchanged, and, indeed, none is observed in our maps. Ascorbate thus effectively mitigates specific oxidative damage. Interestingly, however, the resulting ascorbyl radical, which has been thoroughly characterized previously (Laroff *et al.*, 1972), can be further oxidized to dehydroascorbate (A). This extremely electrophilic species will readily accept electrons, since its alternate route to stabilization in solution, the formation of a cyclic hemiacetal, is presumably hindered at cryotemperatures.

Several other features of our results are pertinent to efforts to understand and quantify radiation damage. The metrics used to judge the extent of global damage here, I/I_0, R_d and *B*-factor (S_{AD}), all gave different results for the relative efficacy of the scavengers, and this underlines the importance of thoroughly exploring the choice of metric. The $I/\sigma(I)$ metric was not utilized since it is inherently unreliable: as the damage increases, the noise also increases and thus biases this parameter. In the present work, crystals soaked in sodium nitrate for 4 or 8 min and irradiated at different dose rates showed varying behaviour regarding their susceptibility to radiation damage depending on the metric used to judge the dose tolerance. While the 'nitrate I4' and 'nitrate II4' crystals showed a significantly higher $D_{1/2}$ than the native, the 'nitrate III8' crystal yielded similar results to the native crystal. Conversely, when the R_d factors were compared across all the crystals, only for 'nitrate I4' was the value of R_d not reduced relative to that of the native.

However, the specific damage indicators consistently showed that all nitrate-soaked crystals exhibited disulfide reduction at much higher doses than did the native crystal. From previous scavenger studies it is clear that the dose tolerance results for scavenger-soaked and co-crystallized samples can vary between crystals nominally grown under identical conditions and treated in the same way; this feature of scavenger studies has already been amply demonstrated by Nowak *et al.* (2009). Thus statistically significant numbers of crystals must be analysed under each set of conditions to enable reliable conclusions to be drawn. Here, only one native crystal was analysed, but comparison with native HEWL crystals from previous work where doses were quoted

[10 MGy (Teng & Moffat, 2000; Weik *et al.*, 2002) and 13 MGy (Davies, 2008)] demonstrates that native HEWL crystals have approximately the same $D_{1/2}$ for global damage as determined in the present work, supporting the evidence that the higher dose tolerance of 'asc' and 'nitrate II4' is due to scavenger effects and not to crystal heterogeneity.

In conclusion, in terms of radiation mitigation strategies, scavenger investigations are definitely worth pursuing since they can give factors of up to two increase in dose tolerance for global damage and up to a factor of six in protecting against specific structural damage at cryotemperatures. It is technically straightforward and thus compares favourably with other approaches. For example, carrying out diffraction experiments at 15 K using helium cryogen, which gave a 23% increase in dose tolerance for holoferritin crystals (Meents *et al.*, 2007), or at 50 K where a factor of four reduction in disulfide bond breakage has been reported for elastase and cubic insulin crystals concomitant with an increase in dose tolerance of 2.6 and 3.9, respectively (Meents *et al.*, 2010).

In addition, scavengers are particularly effective in reducing specific damage if the chemistry involved is appropriately considered. Here the mechanism of action of two well known scavengers, one reductive, the other oxidative, has been elucidated by a combination of online microspectrophotometry and the analysis of electron density maps. Future experiments including both scavenger types may exhibit synergistic effects; however, competition amongst redox products may reduce potential gains.

The data and models from the nitrate and ascorbate series of datasets have been deposited in the PDB.

We are grateful to the ESRF for beam time under Radiation Damage BAG MX-812 and to John McGeehan, Antoine Royant, Martin Weik and Andrew McCarthy for the valuable assistance with the microspectrophotometry set-up and beamline calibration. Karthik Paithankar is thanked for enlightening discussions on data processing, and Kay Diederichs for useful comments concerning the calculation of $R_{\rm d}$ values. The NDRL is supported by Basic Energy Sciences at the US Department of Energy, grant number DE-FC02-04ER15533. This is document number NDRL-4878. EDlM was supported by the Beca Mixta program (CONACyT) and also acknowledges financial support from Proyecto 102370 (CONACyT).

References

Anbar, M., Alfassi, Z. B. & Bregman-Reisler, H. (1967). *J. Am. Chem. Soc.* **89**, 1263–1264.
Armstrong, D. A. (1990). *Sulfur-Centered Reactive Intermediates in Chemistry and Biology*, edited by K. Chatgilialoglu and K.-D. Asmus, pp. 121–134. New York: Plenum.
Barker, A. I., Southworth-Davies, R. J., Paithankar, K. S., Carmichael, I. & Garman, E. F. (2009). *J. Synchrotron Rad.* **16**, 205–216.
Borek, D., Ginell, S. L., Cymborowski, M., Minor, W. & Otwinowski, Z. (2007). *J. Synchrotron Rad.* **14**, 24–33.
Bourgeois, D., Vernede, X., Adam, V., Fioravanti, E. & Ursby, T. (2002). *J. Appl. Cryst.* **35**, 319–326.
Burmeister, W. P. (2000). *Acta Cryst.* D**56**, 328–341.
Buxton, G. V., Greenstock, C. L., Helman, W. P. & Ross, A. B. (1988). *J. Phys. Chem. Ref. Data*, **17**, 513–531.
Carugo, O. & Djinović Carugo, K. (2005). *Trends Biochem. Sci.* **30**, 213–219.
Cascio, D., Williams, R. & McPherson, A. (1984). *J. Appl. Cryst.* **17**, 209–210.
Cianci, M., Helliwell, J. R. & Suzuki, A. (2008). *Acta Cryst.* D**64**, 1196–1209.
Collaborative Computational Project, Number 4 (1994). *Acta Cryst.* D**50**, 760–763.
Corbett, M. C., Latimer, M. J., Poulos, T. L., Sevrioukova, I. F., Hodgson, K. O. & Hedman, B. (2007). *Acta Cryst.* D**63**, 951–960.
Davies, R. J. (2008). Thesis, University of Oxford, UK.
Diederichs, K. (2006). *Acta Cryst.* D**62**, 96–101.
Emsley, P., Lohkamp, B., Scott, W. G. & Cowtan, K. (2010). *Acta Cryst.* D**66**, 486–501.
Evans, G., Polentarutti, M., Djinovic Carugo, K. & Bricogne, G. (2003). *Acta Cryst.* D**59**, 1429–1434.
Evans, P. (2006). *Acta Cryst.* D**62**, 72–82.
Fioravanti, E., Vellieux, F. M. D., Amara, P., Madern, D. & Weik, M. (2007). *J. Synchrotron Rad.* **14**, 84–91.
Garman, E. (1999). *Acta Cryst.* D**55**, 1641–1653.
Garman, E. F. (2010). *Acta Cryst.* D**66**, 339–351.
Garman, E. F. & Schneider, T. R. (1997). *J. Appl. Cryst.* **30**, 211–237.
Hiroki, A., Pimblott, S. M. & LaVerne, J. A. (2002). *J. Phys. Chem. A*, **106**, 9352–9358.
Holton, J. M. (2007). *J. Synchrotron Rad.* **14**, 51–72.
Holton, J. M. (2009). *J. Synchrotron Rad.* **16**, 133–142.
Homer, C., Cooper, L. & Gonzales, A. (2011). *J. Synchrotron Rad.* **18**, 338–345.
Hope, H. (1988). *Acta Cryst.* B**44**, 22–26.
Hug, G. L., Carmichael, I. & Fessenden, R. W. (2000). *J. Chem. Soc. Perkin Trans. 2*, pp. 907–908.
Jones, G. D., Lea, J. S., Symons, M. C. & Taiwo, F. A. (1987). *Nature (London)*, **330**, 772–773.
Kabsch, W. (2010). *Acta Cryst.* D**66**, 133–144.
Kauffmann, B., Weiss, M. S., Lamzin, V. S. & Schmidt, A. (2006). *Structure*, **14**, 1099–1105.
Kmetko, J., Husseini, N. S., Naides, M., Kalinin, Y. & Thorne, R. E. (2006). *Acta Cryst.* D**62**, 1030–1038.
Laroff, G. P., Fessenden, R. W. & Schuler, R. H. (1972). *J. Am. Chem. Soc.* **94**, 9062–9073.
Leiros, H.-K. S., Timmins, J., Ravelli, R. B. G. & McSweeney, S. M. (2006). *Acta Cryst.* D**62**, 125–132.
Leslie, A. G. W. (2006). *Acta Cryst.* D**62**, 48–57.
McCarthy, A. A., Brockhauser, S., Nurizzo, D., Theveneau, P., Mairs, T., Spruce, D., Guijarro, M., Lesourd, M., Ravelli, R. B. G. & McSweeney, S. (2009). *J. Synchrotron Rad.* **16**, 803–812.
Macedo, S., Pechlaner, M., Schmid, W., Weik, M., Sato, K., Dennison, C. & Djinović-Carugo, K. (2009). *J. Synchrotron Rad.* **16**, 191–204.
McGeehan, J., Ravelli, R. B. G., Murray, J. W., Owen, R. L., Cipriani, F., McSweeney, S., Weik, M. & Garman, E. F. (2009). *J. Synchrotron Rad.* **16**, 163–172.
Meents, A., Gutmann, S., Wagner, A. & Schulze-Briese, C. (2010). *Proc. Nat. Acad. Sci. USA*, **107**, 1094–1099.
Meents, A., Wagner, A., Schneider, R., Pradervand, C., Pohl, E. & Schulze-Briese, C. (2007). *Acta Cryst.* D**63**, 302–309.
Milosavljević, B. H. & Mićić, O. I. (1978). *J. Phys. Chem.* **82**, 1359–1362.
Murray, J. & Garman, E. (2002). *J. Synchrotron Rad.* **9**, 347–354.
Murray, J. W., Garman, E. F. & Ravelli, R. B. G. (2004). *J. Appl. Cryst.* **37**, 513–522.
Murshudov, G. N., Vagin, A. A., Lebedev, A., Wilson, K. S. & Dodson, E. J. (1999). *Acta Cryst.* D**55**, 247–255.
Nave, C. & Garman, E. F. (2005). *J. Synchrotron Rad.* **12**, 257–260.
Nowak, E., Brzuszkiewicz, A., Dauter, M., Dauter, Z. & Rosenbaum, G. (2009). *Acta Cryst.* D**65**, 1004–1006.

Oliéric, V., Ennifar, E., Meents, A., Fleurant, M., Besnard, C., Pattison, P., Schiltz, M., Schulze-Briese, C. & Dumas, P. (2007). *Acta Cryst.* D**63**, 759–768.
Owen, R. L., Holton, J. M., Schulze-Briese, C. & Garman, E. F. (2009). *J. Synchrotron Rad.* **16**, 143–151.
Owen, R. L., Rudiño-Piñera, E. & Garman, E. F. (2006). *Proc. Nat. Acad. Sci. USA*, **103**, 4912–4917.
Paithankar, K. S., Owen, R. L. & Garman, E. F. (2009). *J. Synchrotron Rad.* **16**, 152–162.
Ramagopal, U. A., Dauter, Z., Thirumuruhan, R., Fedorov, E. & Almo, S. C. (2005). *Acta Cryst.* D**61**, 1289–1298.
Rao, D. N., Symons, M. C. R. & Stephenson, J. M. (1983). *J. Chem. Soc. Perkin Trans. 2*, pp. 727–730.
Ravelli, R. B. & Garman, E. F. (2006). *Curr. Opin. Struct. Biol.* **16**, 624–629.
Ravelli, R. B. & McSweeney, S. M. (2000). *Structure*, **8**, 315–328.
Ravelli, R. B. G., Theveneau, P., McSweeney, S. & Caffrey, M. (2002). *J. Synchrotron Rad.* **9**, 355–360.
Rice, L. M., Earnest, T. N. & Brunger, A. T. (2000). *Acta Cryst.* D**56**, 1413–1420.
Rodgers, D. W. (1997). *Methods Enzymol.* **276**, 183–203.
Sarma, R. & Zaloga, G. (1975). *J. Mol. Biol.* **98**, 479–484.
Schuler, M. A., Bhatia, K. & Schuler, R. H. (1974). *J. Phys. Chem.* **78**, 1063–1074.
Shimizu, N., Hirata, K., Hasegawa, K., Ueno, G. & Yamamoto, M. (2007). *J. Synchrotron Rad.* **14**, 4–10.
Sliz, P., Harrison, S. C. & Rosenbaum, G. (2003). *Structure*, **11**, 13–19.
Southworth-Davies, R. J. & Garman, E. F. (2007). *J. Synchrotron Rad.* **14**, 73–83.
Southworth-Davies, R. J., Medina, M. A., Carmichael, I. & Garman, E. F. (2007). *Structure*, **15**, 1531–1541.
Teng, T. & Moffat, K. (2000). *J. Synchrotron Rad.* **7**, 313–317.
Teng, T.-Y. & Moffat, K. (2002). *J. Synchrotron Rad.* **9**, 198–201.
Weik, M., Bergès, J., Raves, M. L., Gros, P., McSweeney, S., Silman, I., Sussman, J. L., Houée-Levin, C. & Ravelli, R. B. G. (2002). *J. Synchrotron Rad.* **9**, 342–346.
Weik, M., Ravelli, R. B. G., Kryger, G., McSweeney, S., Raves, M. L., Harel, M., Gros, P., Silman, I., Kroon, J. & Sussman, J. L. (2000). *Proc. Nat. Acad. Sci. USA*, **97**, 623–628.
Weiss, M. S., Panjikar, S., Mueller-Dieckmann, C. & Tucker, P. A. (2005). *J. Synchrotron Rad.* **12**, 304–309.
Wisniowski, P., Carmichael, I., Fessenden, R. W. & Hug, G. L. (2002). *J. Phys. Chem. A*, **106**, 4573–4580.
Yano, J., Kern, J., Irrgang, K. D., Latimer, M. J., Bergmann, U., Glatzel, P., Pushkar, Y., Biesiadka, J., Loll, B., Sauer, K., Messinger, J., Zouni, A. & Yachandra, V. K. (2005). *Proc. Nat. Acad. Sci. USA*, **102**, 12047–12052.
Zaloga, G. & Sarma, R. (1974). *Nature (London)*, **251**, 551–552.